Optimization of Direct Drive Designs for a Proposed Dual Direct/Indirect Drive Laser

Meghan Marangola

Brighton High School

Rochester, NY

Advisor: Dr. R. Stephen Craxton

Laboratory for Laser Energetics

University of Rochester

Rochester, NY

May 2023

1 Abstract

This work investigates the possibility of amending the design of a proposed octahedral laser system to allow for direct drive. Lan et al. proposed this design, which is configured for indirect drive and uses a spherical hohlraum as opposed to a cylindrical hohlraum. The target chamber has 48 quads, each comprised of four laser beams; beams enter the hohlraum through six laser entrance holes. In the amended design, minor changes are made to beam port locations and the laser beam pointings are adjusted for direct drive. The 2-D hydrodynamics simulation code SAGE was used to optimize the pointings. Various beam spatial profiles and radii were investigated. Designs were found with nonuniformity values as low as 0.57% rms, which are comparable to simulations for a similar system (UFL-2M) under construction in Russia. Tuning scans provide a preliminary estimate of the required system pointing accuracy. These results show that the amended design promises high-quality spherical direct drive implosions.

2 Introduction

High uniformity values are essential for achieving ignition through inertial confinement fusion (ICF) of a spherical capsule. ICF is the process of heating up and compressing a capsule in an attempt to create nuclear fusion reactions. Capsules are spherically shaped and typically consist of plastic or glass shells filled with deuterium and tritium, two isotopes of hydrogen. A typical capsule diameter is a few millimeters. The two types of laser-driven ICF are known as direct drive and indirect drive. In direct drive, as shown in Fig. 1, the laser beams hit the capsule directly (Step 1), after which the shell ablates outward, causing the center of the capsule to compress inward (Step 2). Then, the fusion reactions are ignited in the center of the capsule (Step 3), after which alpha particles from the initial fusion reactions are deposited in the surrounding fuel, leading to a propagating burn (Step 4).

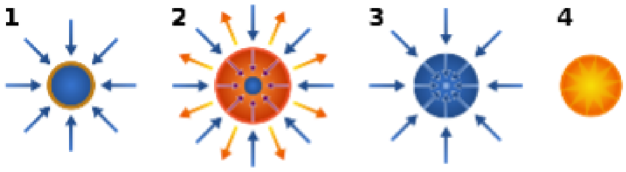

Figure 1: Diagram depicting the process of direct drive inertial confinement fusion. The blue circle is the capsule, with the blue arrows representing the laser irradiation. The fourth image represents the capsule reaching thermonuclear burn.

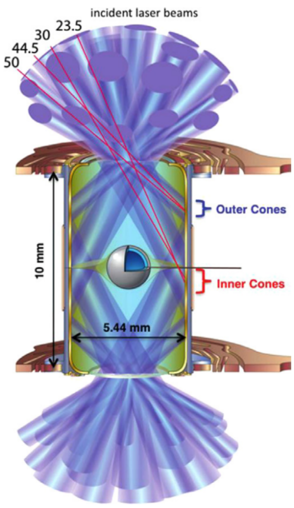

Figure 2: Diagram depicting lasers entering a cylindrical hohlraum, heating up its walls. X rays from the heated hohlraum then irradiate the capsule, shown by the gray sphere. The gold vertical cylinder is the hohlraum. The laser beams are shown in dark blue. Figure from [1].

Indirect drive fusion, as shown in Fig. 2, utilizes a hohlraum, which is usually made of gold. Lasers enter the hohlraum through laser entrance holes (LEH's) at the top and bottom of the hohlraum, and deposit energy onto its inner walls. The energy heats up the walls, which emit x rays that then irradiate the capsule inside.

Until now, indirect drive lasers have been designed for use with cylindrical hohlraums. Because the two LEH's for cylindrical hohlraums are separated by 180°, the optimal beam configuration on the target chamber is to concentrate the beams around two poles across from one another. However, in lasers designed to achieve uniform direct drive irradiation, laser ports are evenly spaced around the target chamber. No lasers have been designed for both direct drive and indirect drive with a cylindrical hohlraum because of the difference in optimized configurations of laser beams around the target chamber. Laser systems like the National Ignition Facility (NIF) are designed for use with cylindrical hohlraums. Although some lasers can run both types of shot, albeit not with optimum efficacy, every multibeam laser that exists today was designed for either indirect or direct drive.

Lan et al. [2] have proposed a design that uses indirect drive through a spherical hohlraum with six LEH's, also referred to as an octahedral hohlraum because the LEH's lie on the vertices of an octahedron. This hohlraum design, pictured in figures 3 and 4, is a sphere with six LEH's that are positioned as if centered on the faces of a cube. The cubic geometry of the hohlraum is highlighted by the outline of the cube in Fig. 3, which makes it easier to visualize the superimposition of the cube onto the surface of the sphere.

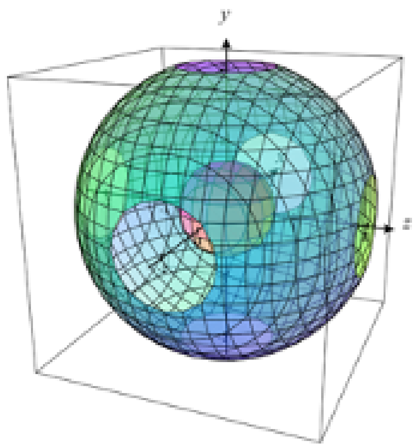

Figure 3: Diagram of an octahedral hohlraum, where the larger sphere with holes represents the hohlraum, the inner sphere represents the capsule, and the cube illustrates the cubic symmetry of the geometry.

The laser that Lan et al. proposed has 48 beams, eight of which would enter each laser entrance hole during a shot, as in Fig. 4. The geometry also works with 48 quads, which are groups of four beams that are more functional on a larger laser system like the NIF. The beams are arranged on six rings in the target chamber, which are 55° from the normal line to each LEH. While there are more LEH's than there would be for a cylindrical hohlraum, the design allows for smaller LEH's. The beam sizes in the LEH plane are constrained by the requirement that the total power per unit area should not exceed the threshold for laser-plasma instabilities. Thus, the area of the spherical hohlraum that is open is the same as that for the cylindrical hohlraum, and to lowest order there are no significant differences in the total energy loss.

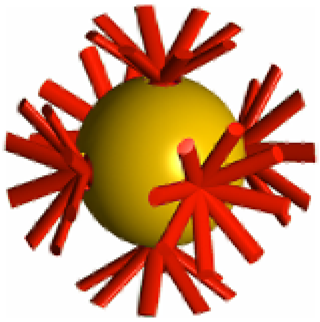

Figure 4: Diagram depicting laser beams (red) entering a gold octahedral hohlraum around an indirect drive capsule, from [3].

2.1 Lan and Amended Lan Configurations

The Lan beam configuration is shown in Fig. 5a. First note the geometry of the diagrams themselves; the spheres are shown in two dimensional images, where due to the stretched display the entirety of the sphere is visible. The black lines, when in three dimensions, form the cube shown in Fig. 3, and the blue line is circular in three dimensions. The Lan configuration has the beams in the target chamber centered on rings that are offset at 55° from the normal line to the center of the laser entrance hole, for all six LEH's. The beams are color coded by the laser entrance hole to which they correspond. The LEH's are aligned with the faces of the cube, as shown in Fig. 3. The geometry is ideal for indirect drive, as eight beams enter each LEH and disperse evenly about the hohlraum. The laser design proposed by Lan et al. has very good uniformity for indirect drive [2].

However, the beam distribution around the six LEH's, instead of at the poles as for cylindrical hohlraums, hints at the possibility of direct drive use. The cubic edges superimposed on the sphere highlight the concentration of the beams in this geometry near the edges of the cube, and especially near its corners. This is not optimal for direct drive, as the beams will deposit more energy on the corners of the cube than on its faces, and uneven energy deposition leads to higher nonuniformity.

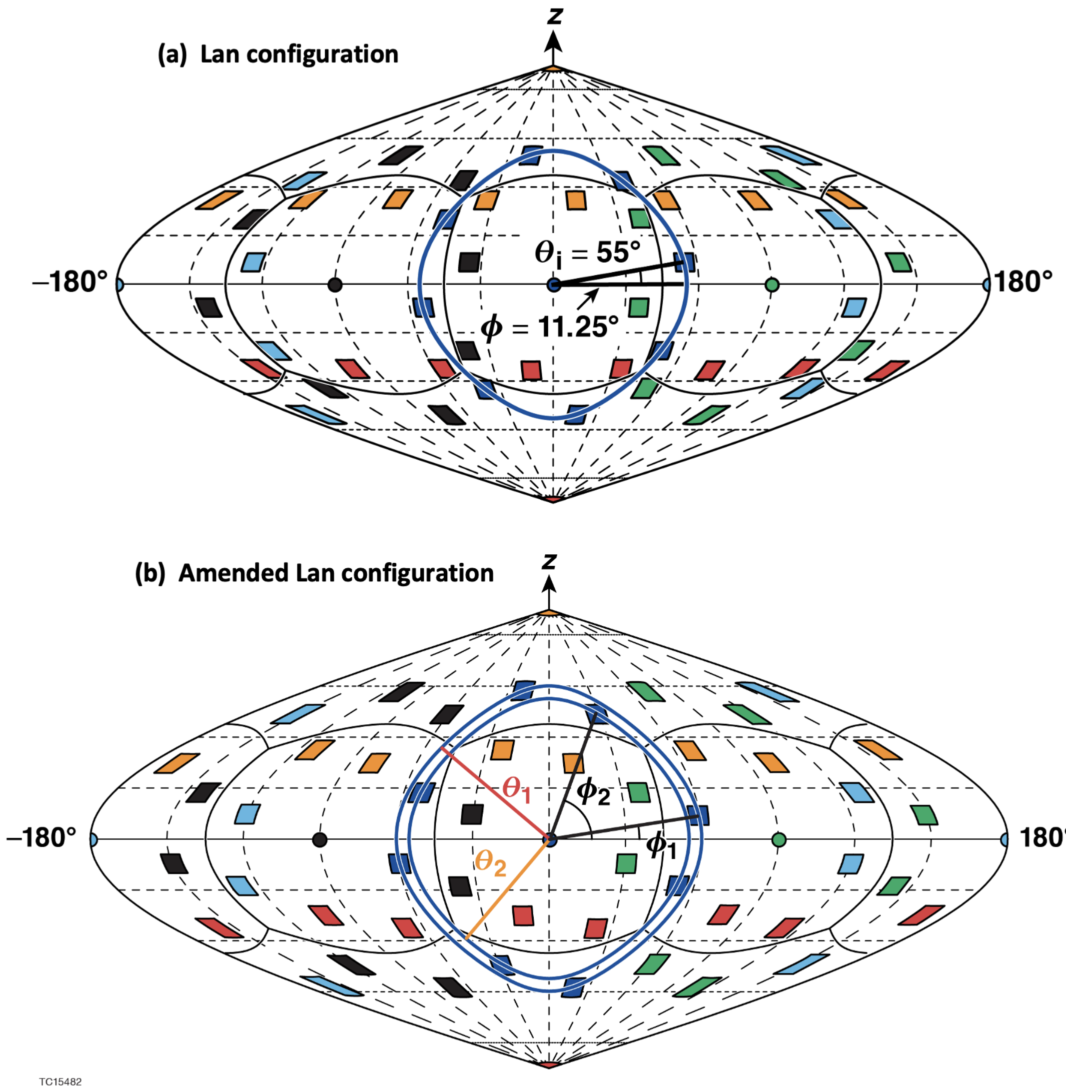

Figure 5: The Lan and amended Lan configurations. Figures (a) and (b) show the locations of the ports on the respective target chambers. The black curves indicate the projection of a cube onto the spherical surface.

Wang [4] worked on an amended configuration shown in Fig. 5b that promises improved direct drive capabilities. The slight differences in beam placement with the amended geometry of Fig. 5b create significant direct drive advantages. Instead of having all beams at a θ offset of 55°, four beams from each ring are shifted to a 60° offset, while the others are left with $\theta = 55°$. Shifting half of the beams creates two groups of 24 beams, with all beams within each group being equivalent. Symmetry requires that each beam can be rotated to four positions on each of the six faces.

In Fig. 5b, the original offset is shown as $\theta_2 = 55°$, while the amended offset for half the beams is $\theta_1 = 60°$. In the other direction, beams with $\theta_1 = 60°$ have $\phi_1 = 11.25°$, while the $\theta_1 = 55°$ beams (every other beam) have $\phi_2 = 45° + 22.5°$. These geometry changes lessen the beam clustering around the corners of the cube and improve the energy deposition on the cube's centers. The amended configuration's indirect drive capabilities match those of the Lan configuration, as shown by Wang [4].

2.2 UFL-2M Configuration

A laser system is under construction in Russia, known as UFL-2M [5] and later as the "Russian laser facility" [6]. It will be referred to as UFL-2M here. This laser was designed for optimum direct drive uniformity and can also be used for indirect drive with an octahedral hohlraum. The target chamber is shown in Fig. 6 and the port configuration in Fig. 7. As for the Lan configuration, the geometry is cubic with 8 beams per cube face. In this configuration all beams are evenly spaced around a cone at 30° from the normal to the cube face [7]. For indirect drive, all beams enter the LEH on the adjacent face of the cube, with an angle of incidence of 62.5° to the LEH normal.

Figure 6: Image of the target chamber of the UFL-2M laser from [8]. The target chamber has a cubic geometry, with 8 beams on each face of the cube.

The configuration has striking symmetry, indicating its potential for direct drive use. A fundamental difference between this configuration and Lan's is that the latter has non-opposing beams, allowing beam dumps like those on the NIF, at which any energy that does not hit the target, including unconverted energy from frequency conversion, would be deposited. In the UFL-2M configuration there are opposing beams where the beam dumps would be. Thus, additional measures are needed for this configuration to prevent energy not absorbed by the target from entering the opposing port and damaging optics.

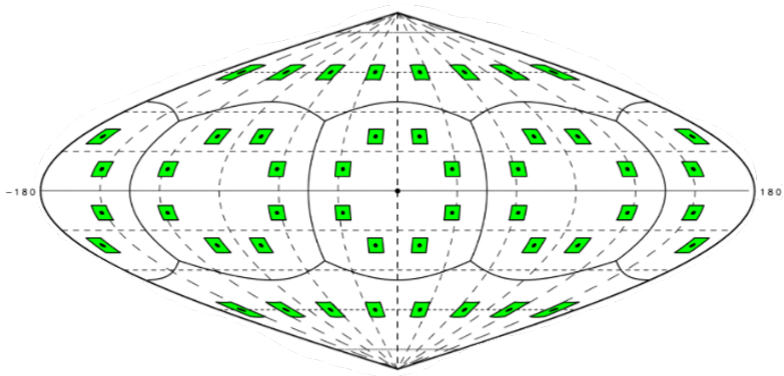

Figure 7: Figure showing the beam ports of UFL-2M overlaid on a sphere.

Section 3 describes the different parameters of the problem and how they contribute to the overall uniformity of the implosions for the 48-beam systems. Section 4 describes the changeable parameters on the 60-beam OMEGA system.

3 Assessment of Direct Drive Uniformity

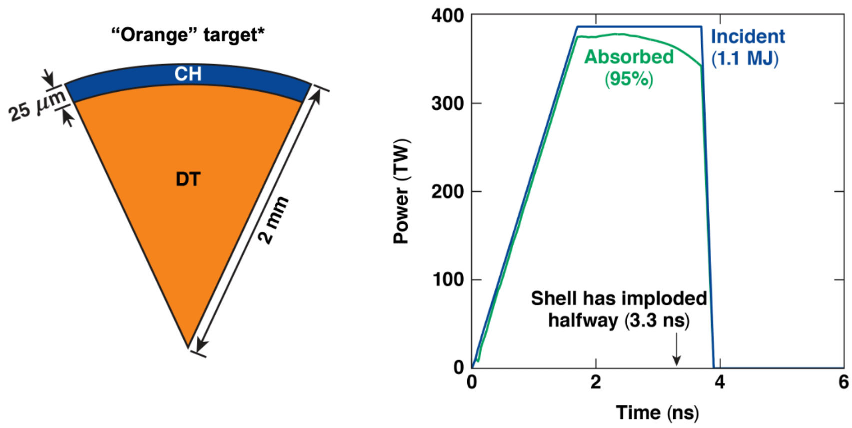

Figure 8: Figure depicting the "Orange" target [9] from NIF shot N190227-001 and the incident and absorbed laser pulses. This target was chosen to compare the NIF and proposed octahedral geometries for direct drive. Figure from [10].

Figure 8 displays a cross-section of the "Orange" target that was shot on the NIF [9] alongside a graph of the beam pulse power and the predicted target absorption. For each shot, there are many parameters that factor in to the uniformity of the implosion. Simulations are helpful in exploring the effects that each parameter has on the uniformity.

The simulations in this paper were run using the 2D hydrodynamics code SAGE [11]. To simulate the configurations, the hydrodynamics was only run in 1D; as the nonuniformities are 3D, there is no advantage to modeling in 2D. However, because the nonuniformity values are low, the simulations in one dimension provide a sufficient approximation of the basic target evolution. Laser deposition is modeled using 3D ray tracing. Laser rays follow curved ray paths along which the ray energy is deposited. The energy is then transported by thermal conduction to the solid density shell, which is accelerated inwards. Deposited energy is stored as a function of θ and ϕ, then integrated over time. Here θ is the angle from the z-axis and ϕ is the azimuthal angle about the z-axis; these angles should not be confused with the angles shown in Fig. 5. The time-integrated 3D deposition patterns are used to characterize the 3D uniformity values, as the root mean square (rms) deviation of this deposited energy σ_{rms} is calculated. As the nonuniformity of the velocity of the imploding shell is $\sim$72% of the deposition nonuniformity [9], the velocity uniformity is better than the deposition uniformity calculated with SAGE. All nonuniformity values reported in this paper are deposition nonuniformity. Many experiments on the NIF have been modeled using SAGE [12] [9].

Section 3.1 describes the parameters that can be controlled using SAGE. Section 3.2 follows, comparing the three 48-beam configurations with center pointing, after which there is a discussion (Section 3.3) on the optimization of the UFL-2M configuration. Then, the optimal parameters for the amended Lan configuration are presented (Section 3.4), followed by a discussion of their sensitivity to changes (Section 3.5). Finally, there is a comparison of the three 48-beam systems for a flat beam setup (Section 3.6).

3.1 Laser Beam Parameters

This section describes problem setups, and defines each of the parameters that were optimized. Results begin in Section 3.2.

3.1.1 Super-gaussian Index

The super-gaussian index is a variable that changes the beam shape. The shapes are governed by the following formula for the beam intensity I as a function of radius r

$$I(r) = I_0 \cdot exp\Big[-\Big(\frac{r}{r_0}\Big)^n\Big], \tag{1}$$

where I_0 is the peak intensity, n is the super-gaussian index, and r_0 is the beam size corresponding to the $\frac{1}{e}$ intensity cutoff. Examples are given in Fig. 9 for $r_0 = 1200$ µm and values of n ranging from 1 to 20.

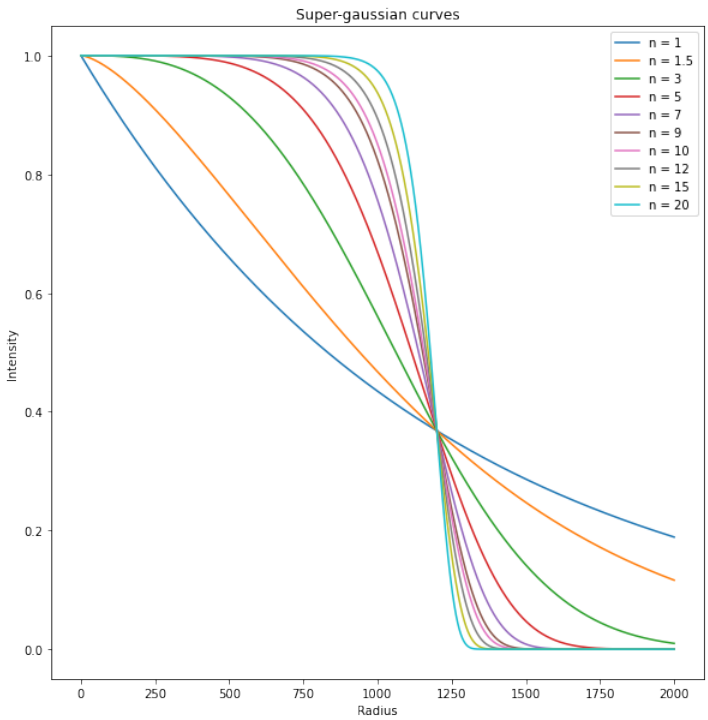

Figure 9: A graph of different super-gaussian beam profiles, with $r_0 = 1200$ µm and a variable n-value.

The variable n controlling the super-gaussian index in SAGE allows the beam spatial profile to be adjusted. With an index of 2, the beam's intensity profile is a simple bell curve; as the n-value increases, the beam drop-off gets increasingly steep, and the intensity plateaus in the center, essentially creating a flat beam. On current lasers the beam profiles are created using phase plates. The runs presented here assume custom phase plates can be designed for future laser facilities.

3.1.2 Beam Radius

The r_0 value corresponds to the beam's radius. With overall increase of the r_0 of the laser beams for a fixed target radius, the uniformity is expected to improve, which is logical; larger beams will have increasing overlap and distribute their energy over a wider area. However, as the beams become larger than the target, more energy misses the target completely and the overall absorption decreases drastically. High energy absorption is desirable due to the high cost of laser energy. Thus, although runs with r_0 significantly larger than the target radius may have considerably lower nonuniformity values, they are both unrealistic and not feasible.

3.1.3 Ray Resolution in SAGE

Within the SAGE code, the user can select the number of rays with which to run each simulation, or the run's "resolution". There are two directions of deposition for the rays, so there are two resolution parameters: number of rays per time step in the r direction, and number of rays in the θ direction, with r and θ here referring to a circular grid in the cross section of the beam. Originally, all runs occurred with 10x12 resolution in r and θ, respectively, taking about forty-five minutes to an hour for each run. As the run resolution increases, the run takes longer, with the longer runs taking up to 12 hours at 40x48 resolution. However, the higher resolution runs give a much more accurate estimate of the nonuniformity and energy deposition patterns, illustrated by the series of runs shown in Fig. 17 (Section 3.5.3). The precision increase from increasing the number or rays is especially important for runs with σ_{rms} values below 1%, as low resolution in the code can be misleading when finding the nonuniformity for the shot.

3.2 Comparison of the Three Configurations with Center Pointing

To compare the performance of the three 48-beam systems on the same shot metrics, the runs have an r_0 value of 1500 µm, a super-gaussian index of 2.7, and beams with no repointing. The three resulting graphs are shown in Fig. 10.

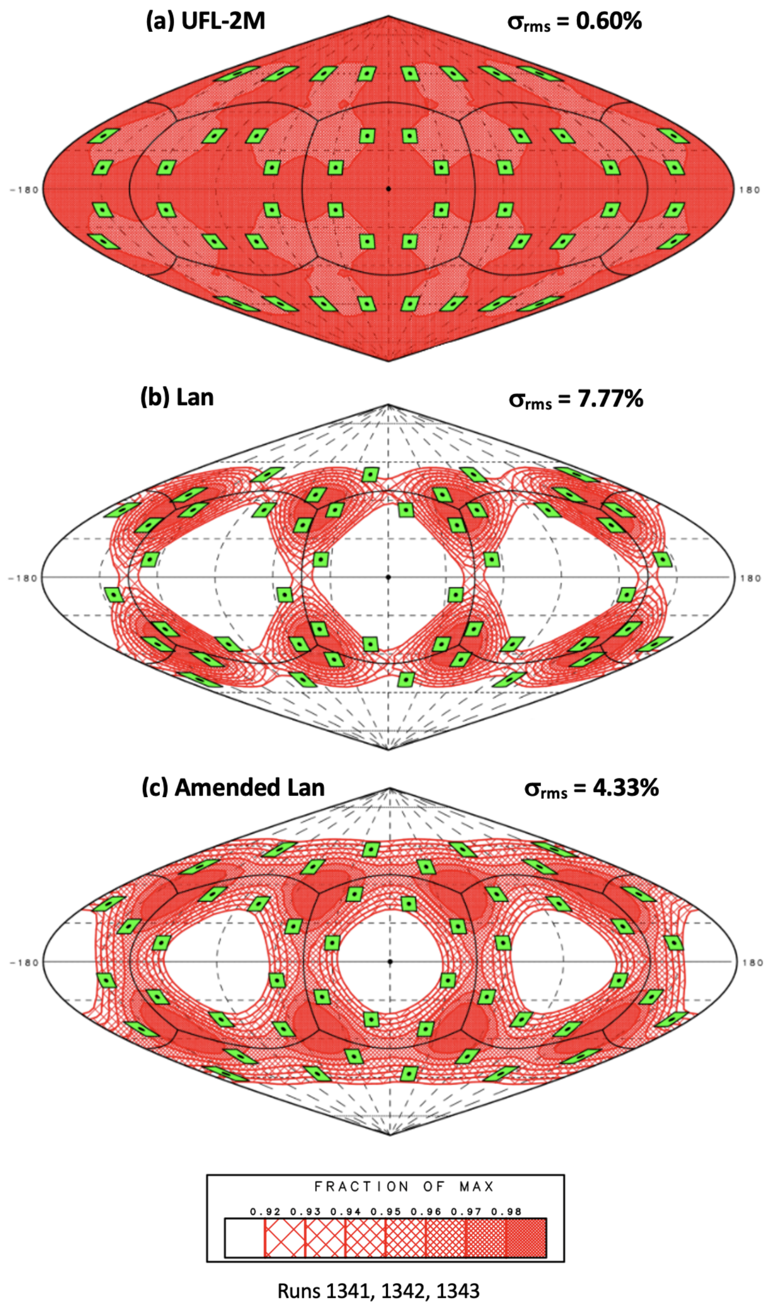

Figure 10: Comparison of contours of time integrated deposited energy for (a) UFL-2M, (b) Lan, and (c) amended Lan configurations with super-gaussian index n of 2.7, beam r_0 of 1500 µm, and center pointings. These plots may be compared with figure 19 (a), (b), and (c), respectively, for n = 15 and $r_0 = 2500$ µm.

As in Figure 5, these figures are 2D representations of spheres. The θ angle measures from the top (north pole) in the vertical direction, while ϕ measures in the horizontal (azimuthal) direction. As shown in the legend, the red shading on the graphs represents the fraction of the maximum energy deposited at each point, and the contour levels range from 92% to 98% of the maximum. The green rectangles represent the locations of the ports on the target chamber, while the black dots represent the aim points of the laser beams. In this case, the black dots align with the centers of the ports because the beams are center pointed. The black outline shows the edges of the cube, a 3D version of which is shown in Fig. 3.

The UFL-2M system performed the best with the lowest σ_{rms} (0.60%), while both the proposed and amended Lan configurations have much higher nonuniformity. As mentioned in Section 2.1, the beams are clustered around the corners of the cube when the Lan configuration is used for direct drive, resulting in significantly less energy deposited in the centers of the cube's faces and a σ_{rms} of 7.77%. The amended design was intended to mitigate some of that effect and improves the uniformity by 3%, to σ_{rms} of 4.33%. However, it is clear that the Lan and amended Lan configurations need significant repointing to achieve more uniform implosions, while the UFL-2M configuration has very low nonuniformity with no correction.

3.3 Optimization of the UFL-2M Configuration

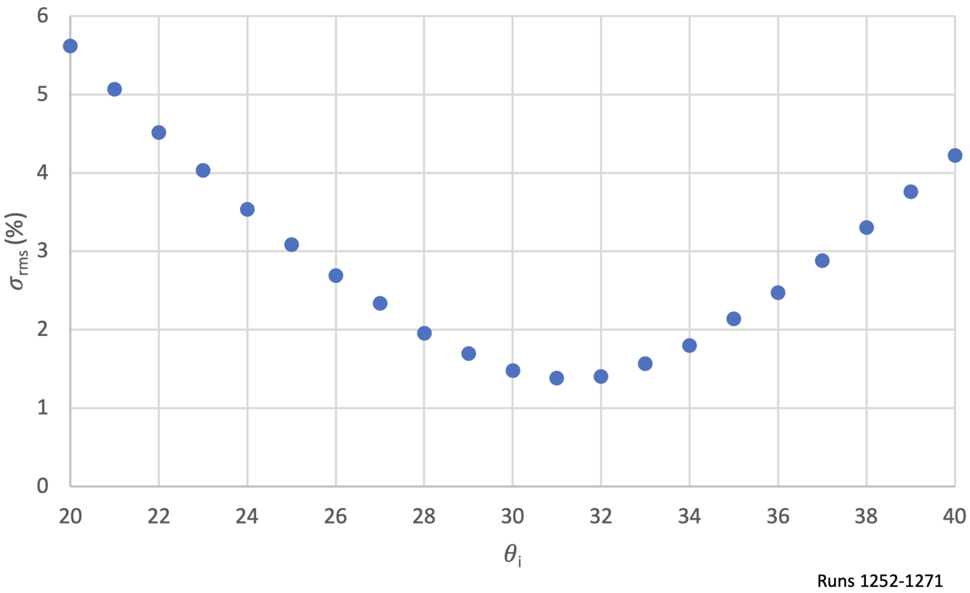

Figure 11: Optimization of the UFL-2M system at center pointings, with super-gaussian index n of 4.7 and r_0 of 1500 µm. θ_i is the angle between the beam direction and the normal to the cube face, and σ_{rms} is the nonuniformity of the time-integrated deposited energy.

To test the UFL-2M system, the θ value of the ports – the angle between the normal and the cube face as described in Section 2.2 – was varied, with no beam repointing. As displayed in Fig. 11, 30° (as found in [7]) is a good port angle to minimize σ_{rms}, but 31° is slightly better. The optimum 30° port angle found in [7] was for a completely different target design and for a shot using green laser light instead of UV. The convergence of optima suggests that the 30° result is more a property of the geometry than of the target design. The geometry of UFL-2M at center pointing achieves very uniform results, meaning no pointing adjustment is necessary.

3.4 Optimization of the Amended Lan Configuration

Given a configuration with the beam port locations on the target chamber fixed, beams can be repointed to improve the uniformity. Similar to the four port angles (θ_1, θ_2, ϕ_1, ϕ_2) introduced in Section 2.1 and shown in Fig. 5b, there are four pointing variables (θ_1', θ_2', ϕ_1', ϕ_2', corresponding to aim points on the initial target surface) in the amended

Lan configuration that can be adjusted in SAGE. One corresponds to the θ value for each set of beams on a 55° ring, one for the θ value for the 60° ring, and one ϕ value for each set of rings. The initial pointings experimented with in this work were those from [4] of $\theta_1' = \theta_1 + 8.5°$, $\theta_2' = \theta_2 + 7.1°$, $\phi_1' = \phi_1 - 0.2°$, and $\phi_2' = \phi_2 - 0.2°$; the run used a super-gaussian index of 3, an r_0 of 1100 μm, and a 10x12 run resolution, which gave a nonuniformity value of $\sigma_{rms} = 1.06\%$. When the angles were changed individually from this set of pointings, none of the changes significantly lowered the nonuniformity. However, combining individual changes that seemed to have slightly opposing effects on the energy distribution patterns created unpredictable and often increasingly nonuniform results. Small changes in the beam spatial profile led to large increases in σ_{rms} (see Fig. 15 below). A different approach to changing the beam pointings was therefore esssential to achieving high uniformity.

Given that the UFL-2M laser configuration had consistently good uniformity values, the beams of the amended configuration were first repointed to the aim points of the UFL-2M configuration. This corresponded to $\theta_1' = \theta_1 + 2.5°$, $\theta_2' = \theta_2 + 7.5°$, $\phi_1' = \phi_1 + 1.25°$, and $\phi_2' = \phi_2 + 10°$. The values of θ_1, θ_2, ϕ_1, and ϕ_2 are given above in Section 2.1.

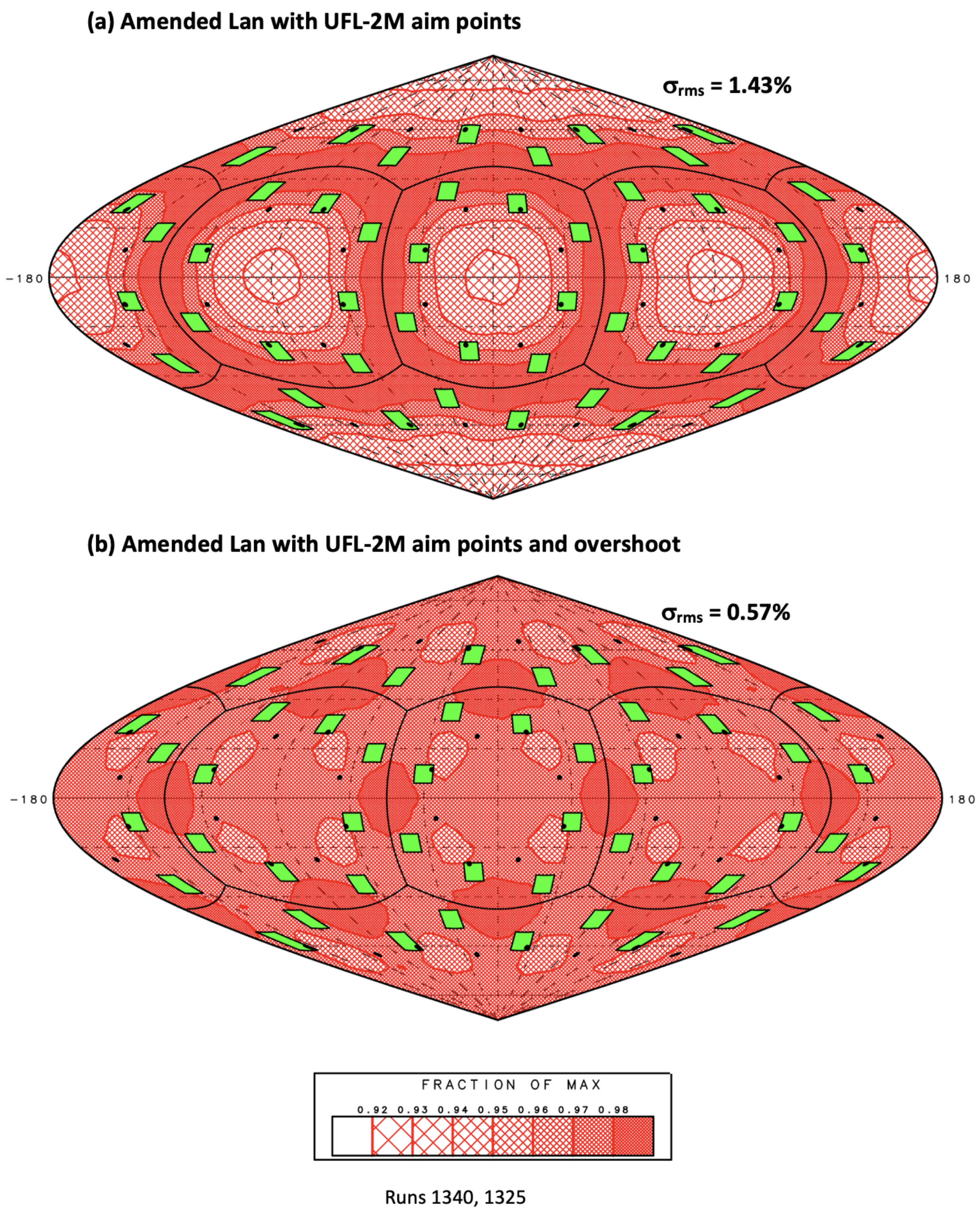

Figure 12: Deposited energy plots for the amended Lan configuration, first repointed exactly to the aim points of the UFL-2M system (a), then with an additional overshoot (b). For both runs, the super-gaussian index n was 2.7 and r_0 was 1500 µm.

The nonuniformity of this simulation, shown in Fig. 12a, was greatly improved at 1.43% (down from 4.33% in Fig. 10c), but remained much higher than the UFL-2M value of 0.60%. The beams of the amended Lan configuration needed further repointing to get the center of the beam energy deposition aligned with the ideal UFL-2M aim point. The optimum configuration, shown in Fig. 12b, was found by increasing the angle shifts by various fractions of the original shifts. The ideal angle ended up being $\frac{1}{3}$ of the way beyond the UFL-2M aim points, with $\theta_1' = \theta_1 + 3.333°$, $\theta_2' = \theta_2 + 10°$, $\phi_1' = \phi_1 + 1.667°$, and $\phi_2' = \phi_2 + 13.333°$. Thus, the total repointing angle for each odd beam (a combination of the θ and ϕ shifts, measured along a great circle) was 3.64°, and for each even beam was 15.25°. These angles are significantly less than the maximum shift of $\sim 37°$ used for the 4 mm NIF design [9] of Fig. 8.

3.5 Sensitivity of the Amended Lan Configuration to Parameter Variations

3.5.1 Super-Gaussian Index

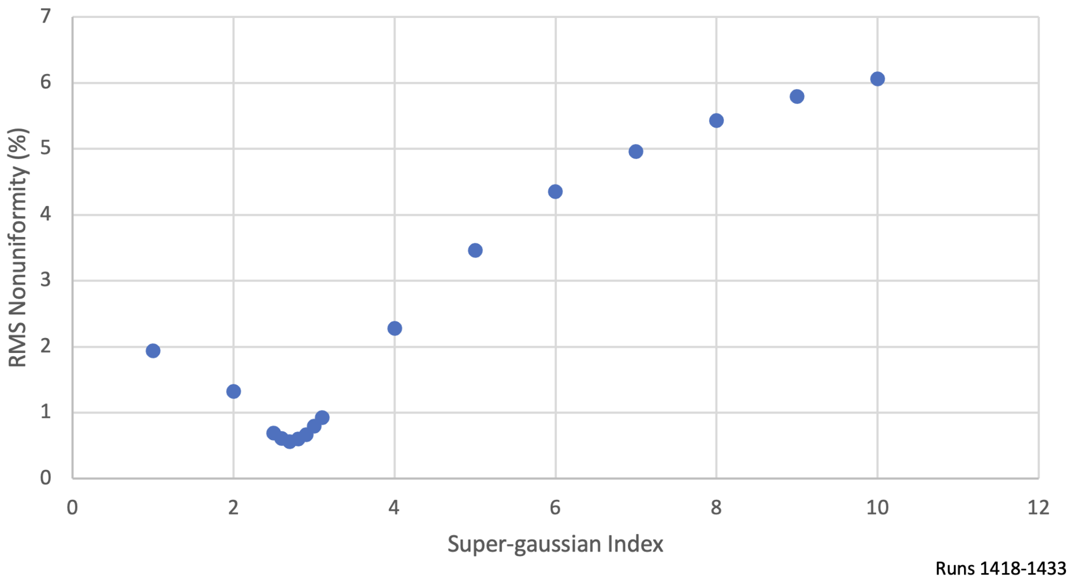

Figure 13: Plot showing changes in RMS nonuniformity due to different super-gaussian indices, with the direct drive pointings used by Wang [4], r_0 of 1100 µm, and resolution of 40x48.

An initial survey of the sensitivity of the amended Lan configuration to the super-gaussian index was carried out using the direct drive pointings and beam radius ($r_0 = 1100$ µm) selected by Wang [4]. The results are shown in Fig. 13, where the radius r_0 and pointings were held constant for all the runs, with a sweep of different index values. The super-gaussian index value of 2.7 yielded the best performance. These results suggest that future phase plates should shape the beam to a super-gaussian with an n-value of 2.7.

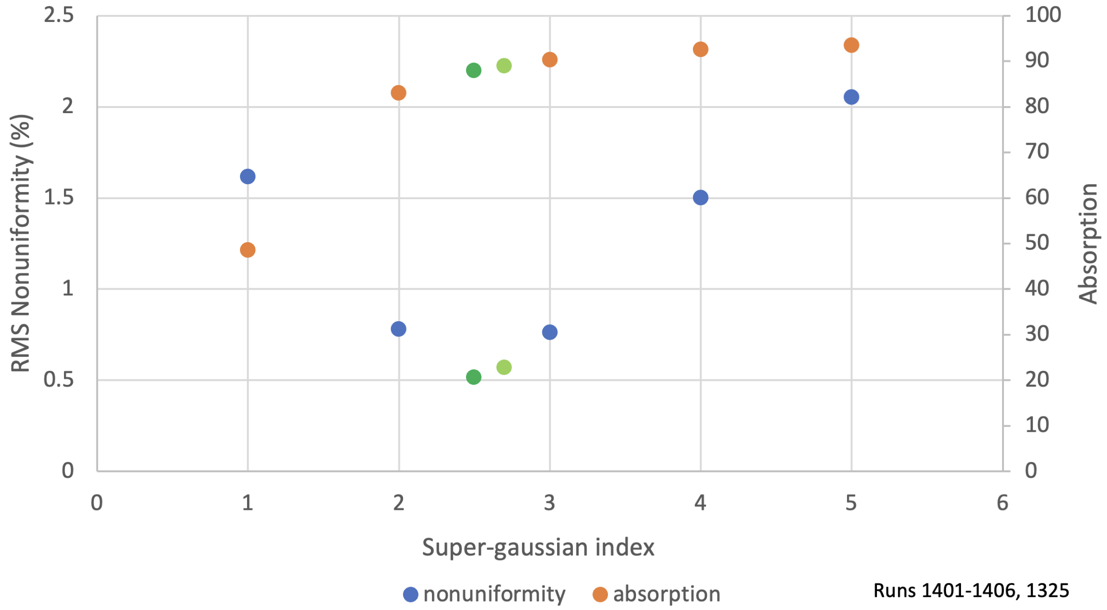

Figure 14: RMS nonuniformity and absorption changes with different super-gaussian indices around the original optimal run from Fig. 12b (n=2.7, shown in light green), with r_0 held constant at 1500 µm. The original optimal run has $\sigma_{rms} = 0.57\%$ and absorption of 88.96%, while the second optimal run (n=2.5, dark green) has $\sigma_{rms} = 0.52\%$ and absorption of 87.91%.

Figure 14 shows a similar plot, but for variations of n around the optimal run of Fig. 12b. The super-gaussian index n on the optimal run was 2.7, and when others were tested in Fig. 14, the RMS nonuniformity value increased, with the notable exception of index $n = 2.5$. Note that in both Fig. 13 and Fig. 14, the optimum super-gaussian index converges around n = 2.7, even with different r_0 values. By varying the values of r_0 and n, optimum values of 1500 µm and 2.7 were chosen. The run in dark green with super-gaussian index $n = 2.5$ has a few tenths of a percentage point better uniformity; however, its absorption drops by a percentage point.

3.5.2 Beam Radius

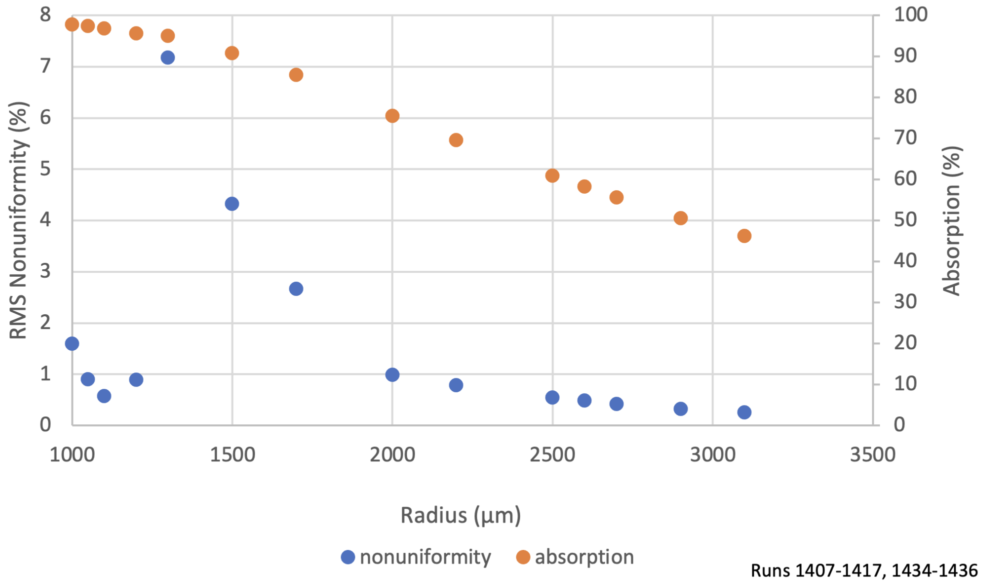

Figure 15: Graph displaying the changes in uniformity with a variable radius r_0, with the direct drive pointings used by Wang [4] and a super-gaussian index of 2.7.

Figure 15 shows the dependence of uniformity on the beam radius r_0, using the pointings selected by Wang [4]. There is a narrow minimum at $r_0 = 1100$ μm with good uniformity, but small changes in radius result in drastic changes in uniformity, so that this value of r_0 should be avoided. There is also a trade-off in absorption with increase in radius, as more energy is refracted around the edges of the target, which influences the choice of optimal r_0.

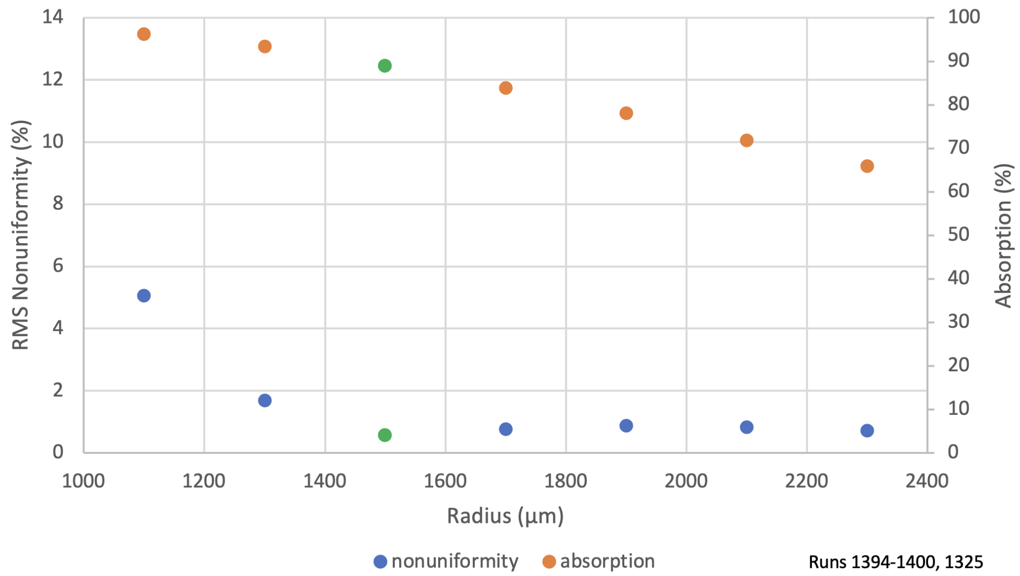

Figure 16: Graph displaying the changes in uniformity and absorption with a variable radius r_0, with the optimal direct drive pointings used for Fig. 12b and a super-gaussian index of 2.7. The optimal run is shown in green, and has an r_0 of 1500 µm.

Figure 16 demonstrates how changes in r_0 around the optimal run affect both the σ_{rms} value and the absorption; the nonuniformity significantly increases with a smaller r_0 value, and there is lower absorption with larger r_0.

3.5.3 SAGE Run Resolution

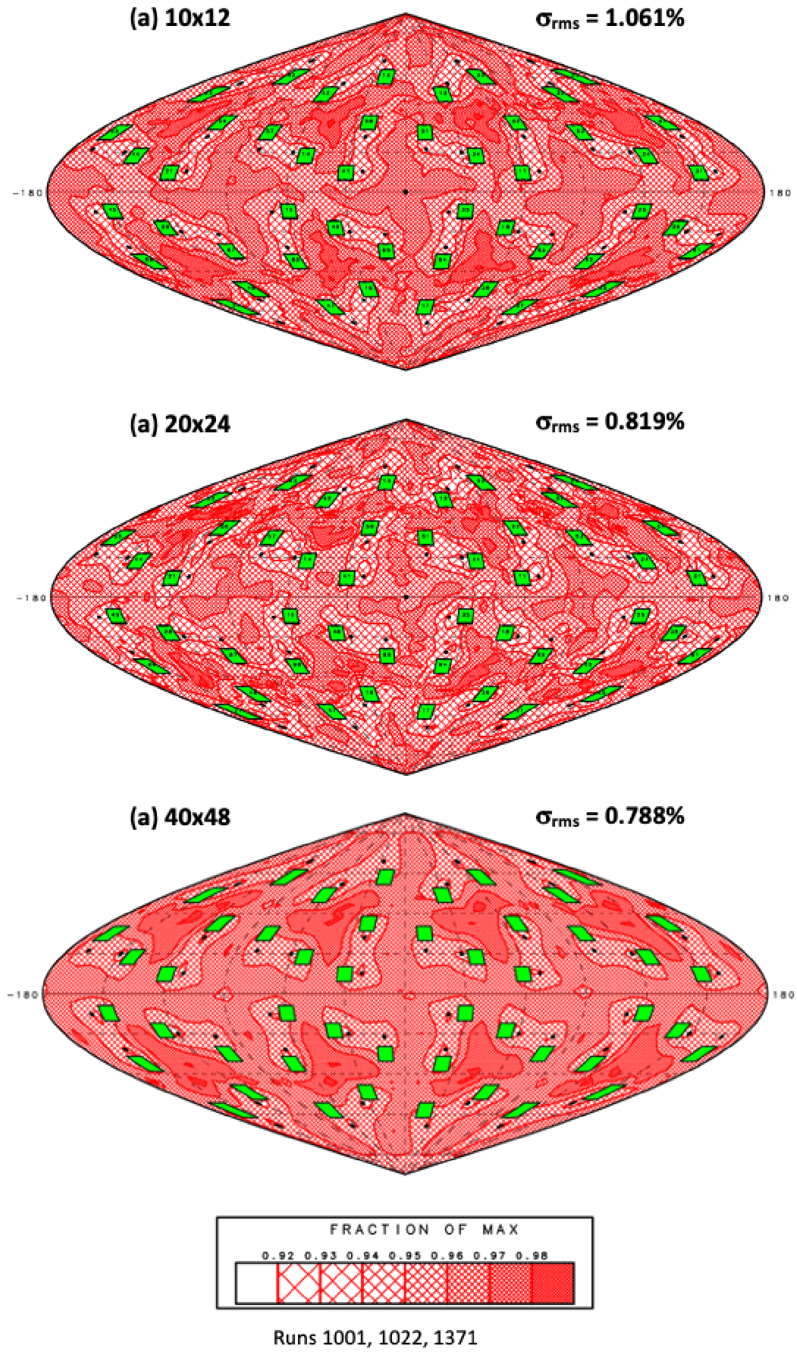

Figure 17: Deposited energy for three runs with identical pointings, super-gaussian index of 3, and r_0 of 1100 µm, but different resolutions.

The runs shown in Fig. 17 are identical aside from the resolution at which they were run. Not only does the nonuniformity drop from the original 1.061% to 0.788%, but the pattern in the highest resolution image is much clearer, which is helpful when trying to improve uniformity. Outside of this section, all of the runs have 40x48 resolution, meaning 40 radial points and 48 angular points from 0 to 180° on the ray grid. For all beams that are shifted in the azimuthal direction, which is the case for most beams, there are 96 angular points from 0 to 360°.

3.5.4 Pointing Accuracy

The sensitivity to beam pointing errors was investigated. By testing many different angle shifts in the direction of the UFL-2M aim points, the sensitivity of the design to pointing errors in that direction was analyzed. The results are shown in Fig. 18 for the even and odd beams.

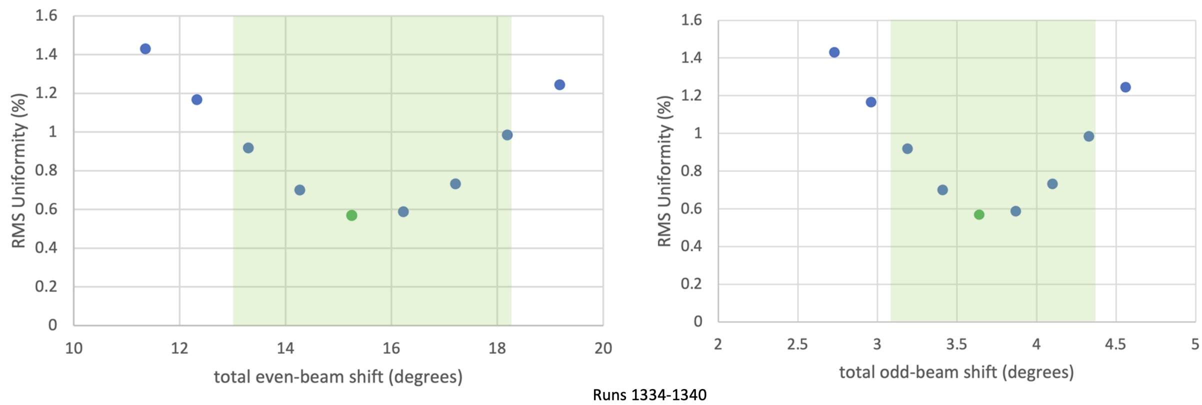

Figure 18: The sensitivity to beam pointing errors for the optimal pointings. The optimum design lies at a relatively robust minimum, with an even-beam shift of 15.25° and an odd-beam shift of 3.64°, displayed as the green point in both graphs.

The design is robust to these changes. As indicated by the green shaded areas, the rms stays below 1% for a range in the total beam shift of 6.5° for even beams and 1.2° for odd beams. It was found that the odd beams require more pointing precision than the even beams. Further runs are required to investigate pointing errors in the orthogonal direction.

3.6 Comparison of the Three Configurations with Flat Beams

Another comparison, though unrealistic, was made between the performance of the three configurations with wide, flat beams, for which the radius was 2500 µm, which is significantly larger than the target radius of 2000 μm. The super-gaussian index was 15. From Fig. 9, the intensity drops off rapidly beyond the radius of the beam, minimizing the loss of target absorption.

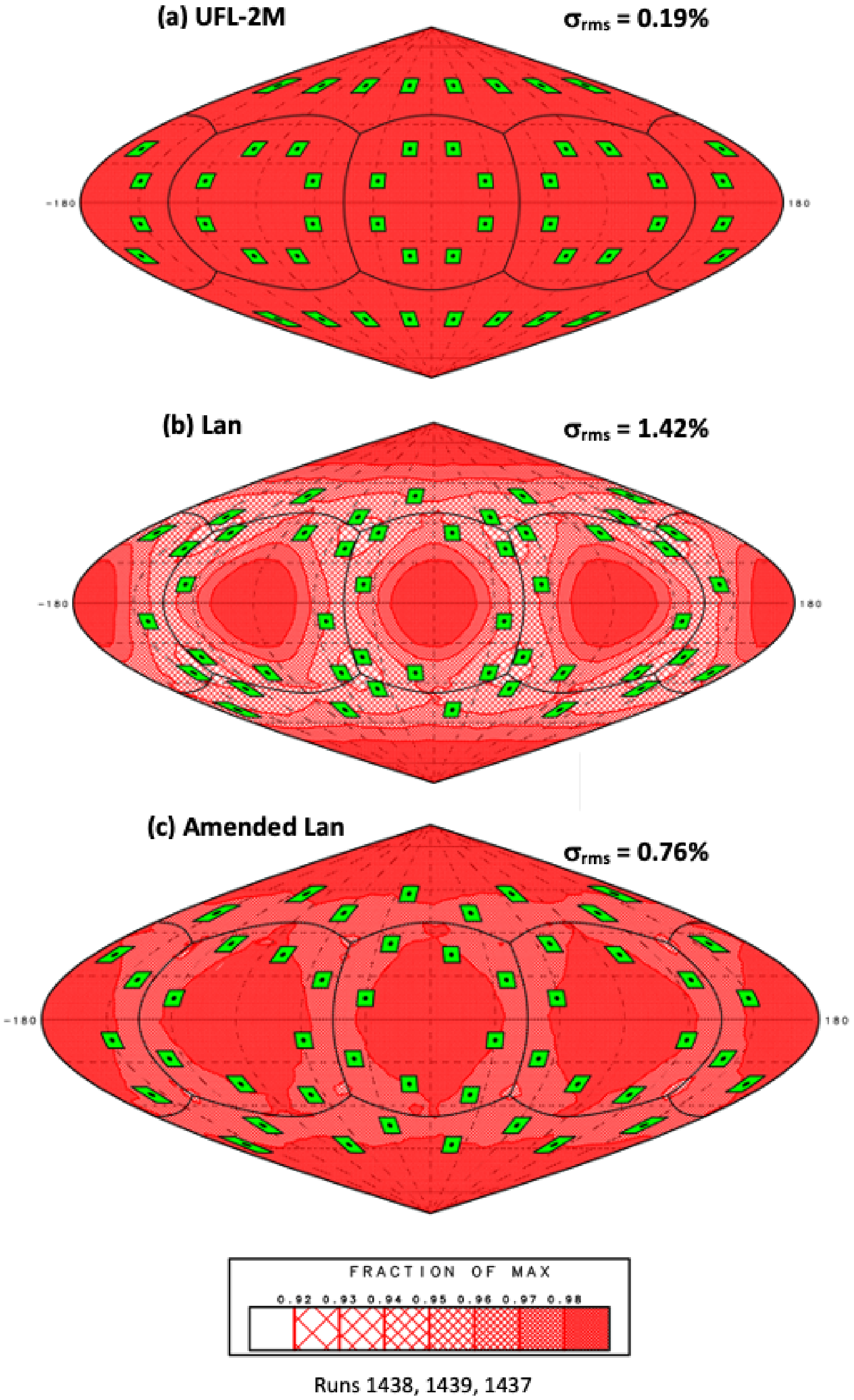

Figure 19: Comparison of the (a) UFL-2M, (b) Lan, and (c) amended Lan configurations with super-gaussian index n of 15, beam r_0 of 2500 µm, and center pointings. The color scale is the same as in Fig. 10 (n = 2.7, r_0 = 1500 µm).

The three plots are all very uniform, with the Lan configuration having the highest nonuniformity of 1.42%, the amended Lan configuration performing slightly better at

0.76%, and the UFL-2M configuration having the lowest nonuniformity of 0.19%. However, as noted in Section 3.1.2, the target absorption decreases significantly with a dramatic increase in radius. Thus, these designs are not viable, because their absorption is only 70%. However, the shots are an interesting exploration of another way to achieve uniformity, and the uniformity comparison confirms that geometrically, the UFL-2M system is the most uniform of the three. In this case, the Lan and amended Lan configurations cannot be compensated by repointing because the beam profiles remain flat.

4 OMEGA Geometry

Simulations with the same target design were also performed for the "stretched soccer ball" geometry used on the Laboratory for Laser Energetics' 60-beam OMEGA laser system. The system's beam ports are arranged on the vertices of a truncated icosahedron, shown in Fig. 20, from [13].

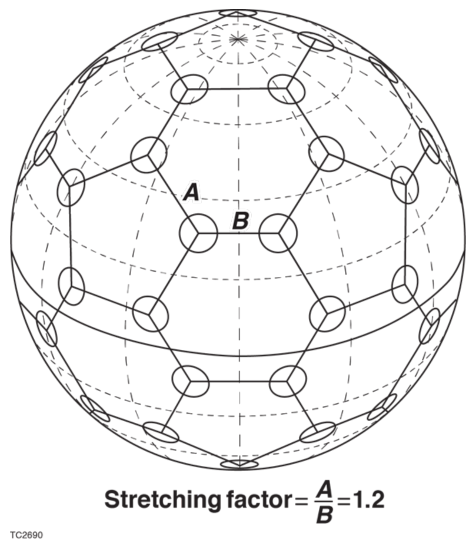

Figure 20: OMEGA laser target chamber geometry. The beam ports are on the vertices of a truncated icosahedron, which has a pattern of pentagons and hexagons.

In an OMEGA-like configuration, there is a stretch factor that goes into the system of ports. This is the ratio of the side lengths of the pentagons and hexagons in the design's geometry, which is $\frac{A}{B}$ in Fig. 20. Normally, the beams in this system are pointed to the center of the target, in which case the aim points on the target also lie on a truncated icosahedron. In this section, SAGE has been used to model what could have been done if OMEGA had been built unstretched – i.e., specified with a stretching factor of 1.0 – but with the beams repointed to the stretched aim points, which in this work is referred to as a pointing stretch factor. The pointing and port stretch factors for OMEGA are 1.2.

4.1 Comparison Runs with 48–Beam Configuration

The problems used to compare the three 48–beam laser configurations in Sections 3.2 and 3.6 were run for the OMEGA geometry as well, as shown in Fig. 21.

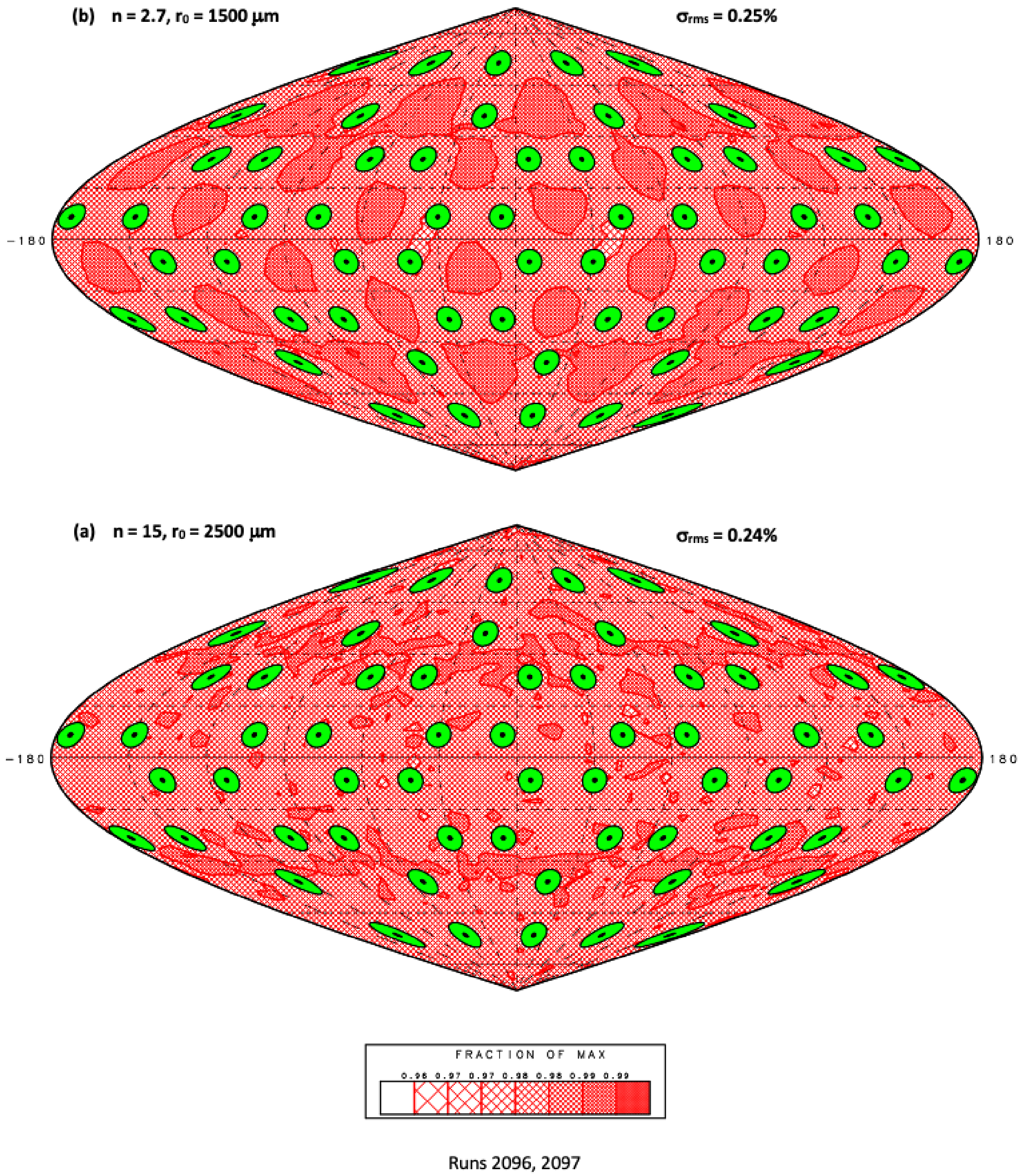

Figure 21: Comparison runs for the OMEGA geometry. (a) is comparable to the runs in Fig. 10 (super-gaussian index $n = 2.7$, $r_0 = 1500$ µm). The OMEGA geometry has the lowest nonuniformity (0.25%, compared with 0.60% for UFL-2M). (b) can be compared to Fig. 19 ($n = 15$, $r_0 = 2500$ µm), with the OMEGA geometry having the second-lowest nonuniformity (0.24%, compared with 0.19% for UFL-2M). Note that identical to the runs in figures 10 and 19, the beams are not repointed.

The OMEGA geometry outperforms all of the 48-beam configurations in the general comparison case (n = 2.7, $r_0 = 1500$ µm), with lower nonuniformity; however, the OMEGA geometry has a slightly higher nonuniformity than the UFL-2M system in the flat beam simulation. As a 60-beam laser designed for direct drive with its beams evenly distributed around the target chamber, OMEGA does have a distinct advantage for realistic super-gaussian beams, but it is interesting to note that the difference between the systems amounts to only a few tenths of a percentage point of nonuniformity.

4.2 OMEGA Geometry Optimization

The OMEGA laser is normally operated with center pointing, meaning both port and pointing stretch factors are equal. However, SAGE can simulate any combination of stretch factors. This section reexamines the choice of optimum stretching factor for OMEGA by running the 4-mm target design for the OMEGA geometry. First, the port stretch factor was held at a constant value of 1.0 while the pointing stretch factor was varied, shown in Fig. 22.

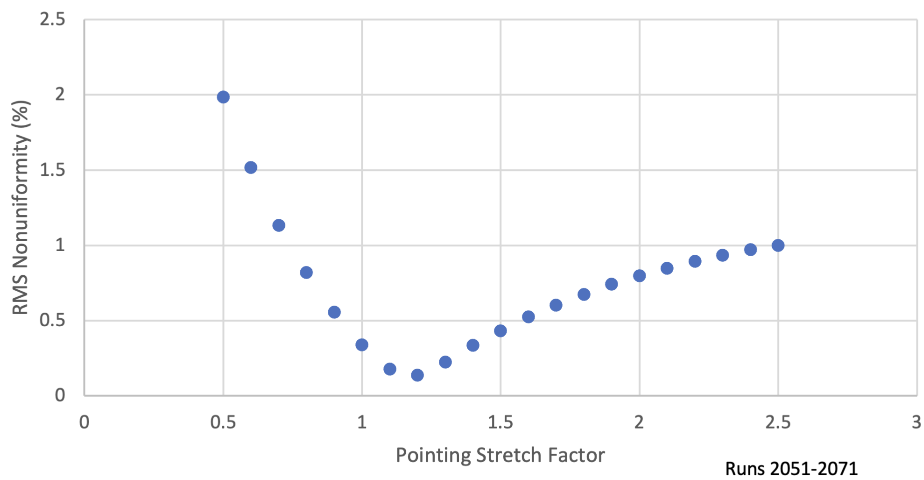

Figure 22: Graph of nonuniformity as a function of pointing stretch factor, with a constant port stretch factor of 1.0, a super-gaussian index of 4.7, and an r_0 of 1700 µm.

The point with the lowest nonuniformity in Fig. 22 is the configuration with the pointing stretch factor of 1.2, with a nonuniformity value of 0.14%. The configuration with port stretch factor of 1.0 and pointing stretch factor of 1.2 would have been optimum if OMEGA had been built with unstretched ports.

Then, the uniformity was tested when both stretch factors were set to the same value, for a variety of values, as displayed in Fig. 23.

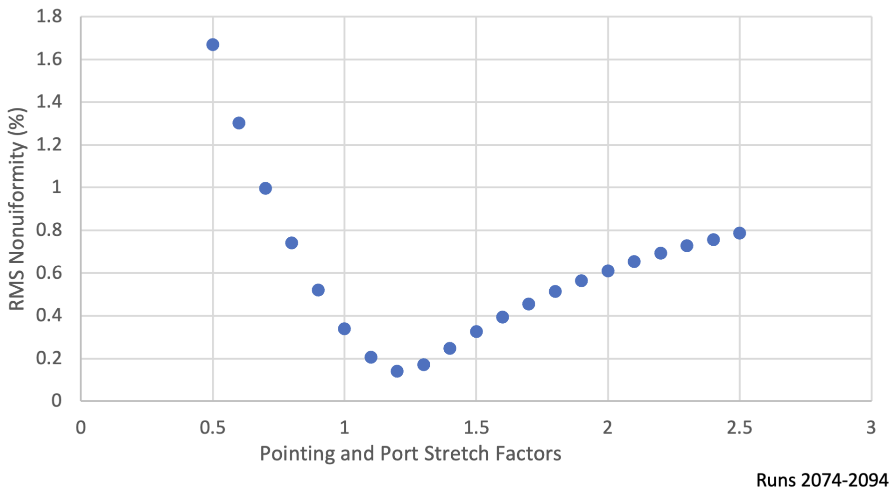

Figure 23: Graph of nonuniformity as a function of simultaneously changing and equal pointing and port stretch factors, with a super-gaussian index of 4.7 and an r_0 of 1700 µm. The minimum σ_{rms} in this graph is 0.17%, which occurs when both stretch factors are 1.2 (i.e., OMEGA as built).

Note that in Fig. 23, the point at stretch factors of 1.2 represents the OMEGA geometry and has the lowest nonuniformity of 0.17%; this value is slightly lower than the value from Fig. 21a (0.25%), for which the super-gaussian index and r_0 were different. These results confirm the rationale behind the choice of OMEGA's geometry; using a completely different target design, the minimum in the σ_{rms} corresponds to the same stretch factor of 1.2. Note that the nonuniformity is lower than for the 48-beam configurations; as mentioned before in Section 4.1, OMEGA was designed for direct drive shots. There is no obvious way the OMEGA geometry can be used for a 60-beam dual direct/indirect drive laser system with favorable angles of incidence to the LEH normals. Although the 48-beam systems have higher nonuniformity for direct drive when compared with the OMEGA geometry, the difference is so small that it may not outweigh the advantages of the 48-beam system.

5 Conclusion

Lan proposed a design for a laser system to be used for indirect drive with an octahedral hohlraum [2], which was then amended by Wang to improve its direct drive capabilities [4]. The 2-D hydrodynamics code SAGE was used to simulate shots on these two laser systems and optimize the pointings and beam spatial profiles. The beams of the amended Lan configuration were repointed to the aim points of the UFL-2M system [5], and then an overshoot was added to optimize. A design was found with a nonuniformity value of 0.57%, comparable to the 0.60% of the UFL-2M system. However, in contrast to UFL-2M, the amended Lan design does not have opposing beams, which may be a design advantage for the system. Pointing scans yielded an approximation of the necessary system pointing accuracy. These results indicate that the amended design will give high caliber spherical direct drive implosions. The OMEGA 60-beam geometry was also investigated, and was found to have only slightly more uniform direct drive results. Thus, if a dual direct drive and indirect drive system is desired, the 48-beam geometry is advocated.

6 Acknowledgements

I would first like to thank Dr. R. Stephen Craxton for directing the high school program and being a patient and insightful advisor. Dr. Craxton was always able to make time to see new results and was an invaluable resource for completing this project. Thank you also to Ms. Truebger for coordinating the finer details. Finally, thank you to the other students for being great company over Zoom.

References

[1] D.E. Hinkel, M.D. Rosen, E.A. Williams, A.B. Langdon, et al. Stimulated Raman scatter analyses of experiments conducted at the National Ignition Facility. *Physics of Plasmas*, 18:056312, 2011.

[2] K. Lan, J. Liu, D. Lai, W. Zheng, and X.-T. He. High flux symmetry of the Spherical Hohlraum with Octahedral 6 LEHs at the hohlraum-to-capsule radius ratio of 5.14. *Physics of Plasmas*, 21(1):010704, 2014.

[3] L. Jing, S. Jiang, L. Kuang, L. Zhang, et al. Preliminary study on a tetrahedral hohlraum with four half-cylindrical cavities for indirectly driven inertial confinement fusion. *Nuclear Fusion*, 57(046020), 2017.

[4] W. Wang. Development of a Beam Configuration for the SG4 Laser to Support both Direct and Indirect Drive. *Laboratory for Laser Energetics*, Summer High School Research Program project report (2019).

[5] V.B. Rozanov, S. Yu. Gus'kov, G.A. Vergunova, N.N. Demchenko, et al. Direct-drive targets for the megajoule facility UFL-2M. *Journal of Physics: Conference Series*, 688:012095, 2016.

[6] N.N. Demchenko, G.V. Dolgoleva, S. Yu. Gus'kov, P.A. Kuchugov, et al. Comparison and analysis of the results of direct-driven targets implosion. *IOP Conference Series: Journal of Phyiscs*, 907:012019, 2017.

[7] N.N. Demchenko, S. Yu. Gus'kov, N.V. Zmitrenko, V.B. Rozanov, and R.V. Stepanov. Uniformity simulation of multiple-beam irradiation of a spherical laser target with the inclusion of radiation absorption and refraction. *Quantum Electronics*, 49:124–132, 2019.

[8] A step closer to thermonuclear synthesis: First module of world's most powerful laser launched in Sarov, Russia, VNIIEF, 2020.

[9] C.B. Yeamans, G.E. Kemp, Z.B. Walters, H.D. Whitley, et al. High yield polar direct drive fusion neutron sources at the National Ignition Facility. *Nuclear Fusion*, 61(046031), 2021.

[10] R. S. Craxton, W. Y. Wang, and E. M. Campbell. A new beam configuration to support both spherical hohlraums and symmetric direct drive. *62nd Annual Meeting of the American Physical Society Division of Plasma Physics*, Nov. 2020.

[11] R. S. Craxton and R. L. McCrory. Hydrodynamics of thermal self-focusing in laser plasmas. *Journal of Applied Physics*, 56(1):108–117, 1984.

[12] A.M. Cok, R.S. Craxton, and P.W. McKenty. Polar-drive designs for optimizing neutron yields on the National Ignition Facility. *Physics of Plasmas*, 15:082705, 2008.

[13] The OMEGA Upgrade - Part II: Preliminary design and target system. *LLE Review*, 39:113–132, 1989.